Editors' Suggestion | Featured in Physics

Effect of wing sweep on a perching maneuver

Dibya Raj Adhikari, George Loubimov, Michael P. Kinzel, and Samik Bhattacharya*
Department of Mechanical and Aerospace Engineering, University of Central Florida, Orlando, Florida 32816, USA

(Received 29 June 2021; accepted 15 March 2022; published 15 April 2022)

While landing, birds often perform a perching maneuver, which involves pitching their wings upward while decelerating to a complete stop. This study is motivated by the observation that some birds fold their wings to create a wing sweep during such perching. The objective of this study is to find out whether such a wing sweep helps during a perching maneuver. We use two flat plates, one with a sweep and another without any sweep, and consider a deceleration maneuver where both of them decelerate to stop from Reynolds number $\mathrm{Re} = 13\,000$. We consider two cases: one, where the wings undergo only heaving, and two, where the wings perform both heaving and pitching. The latter maneuver was designed to mimic perching. By performing experiments and simulations, we compare the temporal evolution of the instantaneous forces and the vortex dynamics of both these plates. We show that during a major part of the deceleration, the instantaneous lift forces are higher in the case of the plate with sweep compared to the plate with no sweep during both kinematics. Our results indicate that the higher lift in the swept plate case was contributed by a stable leading-edge-vortex (LEV) which remains attached to the plate. This increase in stability was contributed by the spanwise vorticity convection caused by a distinct spanwise flow on the swept plate, as revealed by the numerical simulation. We also show that combined pitching and heaving resulted in higher force peaks, and the forces also decayed at a faster rate in this case compared to the heave-only case. Finally, by using an analytical model for unsteady flows, we prove that the higher lift characteristics of the swept plate were entirely due to higher circulatory forces.

DOI: 10.1103/PhysRevFluids.7.044702

I. INTRODUCTION

Natural flyers, such as birds, are known for their agile flight characteristics during different stages of flight. Many of them perform a nimble maneuver, known as perching, which allows them to land smoothly. During this maneuver, they pitch up their wing to a high angle of attack, which has been shown to augment lift and enable a controlled landing [1]. The present study is motivated by this perching maneuver and has two major objectives: one, we want to investigate how a wing sweep influences a perching maneuver; and two, we want to find how does the addition of pitch-up maneuver during a downward deceleration influence the unsteady forces and the flow field.

Perching is a complicated maneuver involving simultaneous pitching, heaving, and deceleration. A number of researchers have investigated the effect of these factors. For example, Polet *et al.* [2] used an airfoil undergoing a simultaneous deceleration and pitching, and investigated the effect of shape change number on the lift production during the terminal phase of deceleration. The shape change number quantifies the rapid area change due to a pitching motion. It has been shown that such rapid area change imparts forces on the body due to added mass effects [3,4] and energy

*Samik.Bhattacharya@ucf.edu

dissipation into the fluid by continuously shedding of vorticity both from the leading and trailing edge.

An unsteady maneuver, such as perching, also depends on the shape of the wing itself. A number of researchers have studied this aspect. Hartloper and Rival [5] examined a rapid pitch-up motion on rectangular, lunate, and truncate planforms and noted that span-wise leading-edge curvature promotes the outboard convection of the vorticity into the wake leading to a favorable lift to drag ratio. Conversely, an experimental work by Granlund *et al.* [6] on pitching rectangular and Zimmerman planforms found a minimal difference in the instantaneous forces and the flow field. In addition, Yilmaz and Rockwell [7] analyzed flow structures on the pitching rectangular and elliptical wings and found a similar vortex structure on both wing shapes. In fact, experimental studies by Berg and Biewenger [8] and Provini *et al.* [9] showed that independent of the wing planforms, birds execute a similar perching maneuver during the landing motion. However, an unsteady maneuver such as rapid pitching is always accompanied by massive separation and the consequent formation of large-scale vortices. Several studies have also investigated the effect of pitch rate on the evolution of vortices [10–13]. It has been known from the research on delta wing that wing sweep stabilizes such leading-edge-vortices. Maxworthy noted that because of the angle between the leading edge and the incoming flow vector, an outward-directed spanwise flow is induced on the delta wing, which stabilized the LEV and delayed the shedding of the vortex [14]. To understand the similar effect of wing-sweep during perching maneuvers, we compare the flow field of a rectangular and swept wing.

Since perching is executed during landing, the effect of ground needs to be taken into account. For smooth landing, it is acknowledged that birds capitalize on the ground effect [15–17]. Ground effect is a phenomenon where the lift to drag ratio of the wing increases when the wing is close to the ground [18,19]. An improvement in the performance due to the ground effect is well documented on many bird's flights [20–22], and it has inspired the development of wing in ground effect aircraft [23]. In the present study, we include the effect of ground in the wing-kinematics by subjecting the wings to decelerate to a stop close to the wall.

While several studies on pitching maneuvers with different planforms exist, very few have combined all the aspects of perching maneuver and considered rapid pitch-up motion while decelerating and descending close to the ground. Therefore, the role of wing planforms on the unsteady aerodynamic mechanism during a true perching flight is yet to be understood in its entirety. In this paper, we consider two types of unsteady motion: (i) heave-down in deceleration and (ii) simultaneous heave-down and pitch-up in deceleration, referred to as perching motion. Heave-down motion is performed to represent the gradual decrease in the ground height, while pitch-up motion is used to represent the rapidly increasing angle of attack (AOA) during the landing maneuver. We performed both experimental and numerical studies to understand flow physics. Finally, results from a two-dimensional analytical model are compared with the experimental result.

II. PROBLEM DESCRIPTION AND METHODS

A. Experimental setup

Experiments were conducted in a free surface towing tank of dimension 0.9 m (L) $\times$ 0.45 m (W) $\times$ 0.4 m (H). Figure 1 illustrates the schematics of the experimental setup. A servo-driven linear stage (FSL120, FUYU Inc., China) was used to tow the wing models along the length of the water tank. The deceleration was applied by gradually slowing down this linear stage. The heaving motion was executed with a stepper-driven linear stage (LSQ150B-T3, Zaber Tech. Inc., Canada) connected orthogonally to the servo-driven stage. The pitching motion was executed with the help of a stepper-driven rotary stage (RSW60A-T3, Zaber Tech. Inc., Canada). The pitch axis was located at the midchord point of both wings. The speed and acceleration of all the linear stages were measured using an ultrasonic motion sensor (PASCO PS-2103A3, USA). The movements of the heaving motor and the pitching motor were synchronized with the forward towing motion with

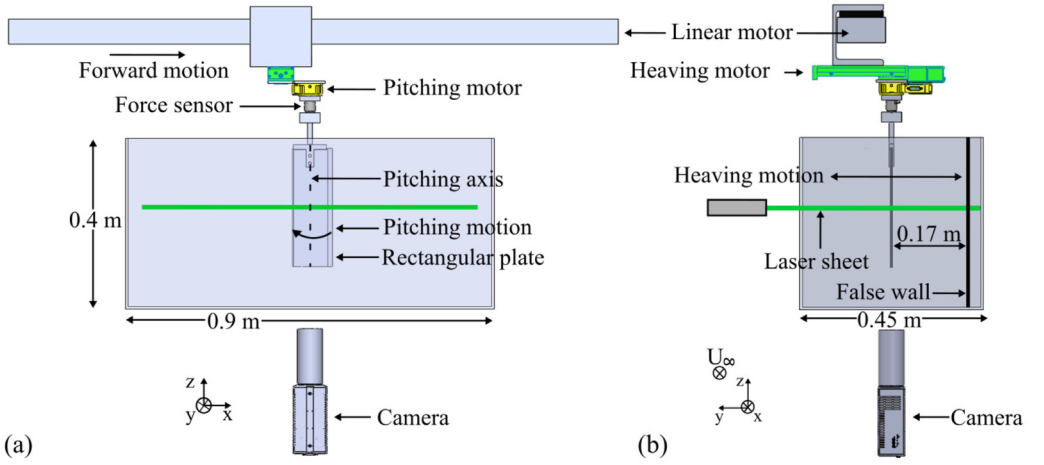

FIG. 1. Schematic diagram of the experimental setup: (a) side view; (b) view from downstream. A smooth ground surface was created by inserting a false wall on one side of the towing tank.

the help of a proximity switch which generated a master pulse to drive the rest of the motors at specified intervals. A force sensor was attached below the pitching motor. The wing model was connected to the force sensor through a cylindrical rod. The wing model was submerged vertically in the towing tank, with 0.09 m gap between the wingtip and the tank bottom.

B. Wing models and kinematics

Two flat plate wing models were used in this study: one with a rectangular planform and another with a swept planform (Fig. 2). Both these wings were fabricated from a 6 mm thick aluminum plate. Moreover, both these plates had the same planform area of 0.03 m^2. The thickness and planform were matched to ensure that both the plates have a mass of 0.46 kg. We matched the mass and the planform area of the plates to ensure that the inertial load on the force sensor and the added mass forces during an unsteady motion are not caused by differences in these parameters. We note, however, that maintaining the same planform resulted in dissimilar chord lengths. The rectangular plate had a chord (c) of 0.1 m. The swept plate had a maximum chord of 0.115 m. It had a sweep angle of 20° starting from the midspan location. The leading-edge of both these plates were rounded while the trailing edges were sharpened to satisfy the Kutta condition.

To simulate a landing flight, two comparable kinematics were considered. In the first case, a wing started a heaving motion from the centerline of the towing tank towards the side-wall, which acted as a ground, while simultaneously decelerating from a steady velocity (U_∞) of 0.1 ms^{-1}.

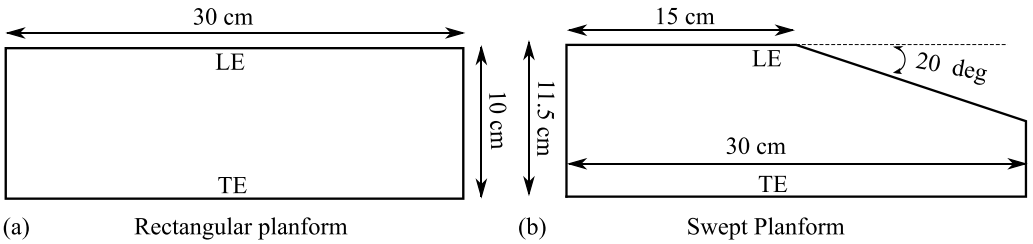

FIG. 2. Wing planform shapes used to study the perching maneuver in landing flight: (a) rectangular planform; (b) swept planform.

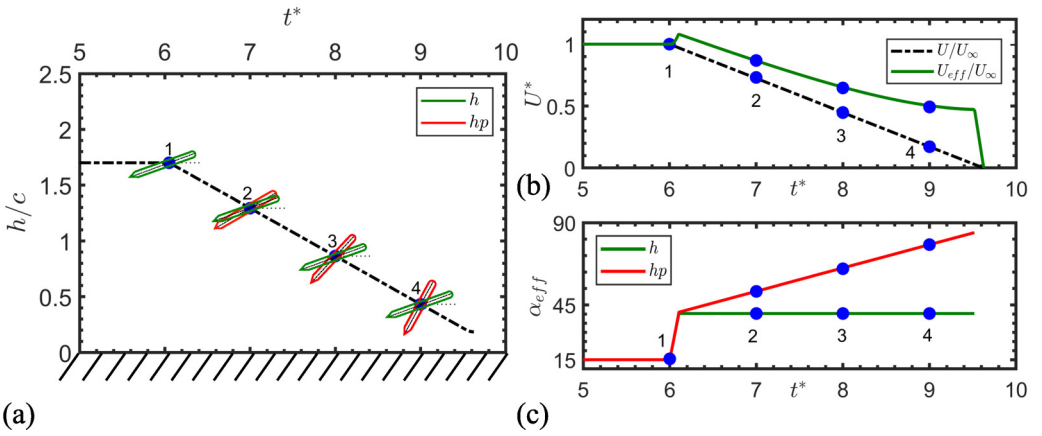

FIG. 3. Details of kinematics: (a) variation of the ground height with t^*, the plate is translating to the right while carrying out heave-only (h) and heave-pitch (hp) motion. Y axis is the nondimensional ground height; (b) variation of the nondimensional free-stream velocity with t^*. Here, the effective velocity, U_{eff}, is defined as $U_{\text{eff}} = \sqrt{U_\infty^2 + \dot{h}^2}$; (c) variation of the effective angle of attack of the plate with t^*. In panels (b) and (c) the variables are plotted as a function of the nondimensional time, $t^* = t\frac{U_\infty}{c}$.

This case will be referred to as the "heave-only" case. In the second case, the wing performed a pitch-up motion while executing the same kinematics as the previous one. This case will be referred to as the "heave-pitch" case. The duration of the heaving and the pitching motions was 3.4 s, which was the same as the duration of the deceleration. In other words, heaving and pitching both started at the same time as the decelerating motion with zero phase difference. We note that only the "heave-pitch" case resembles a perching maneuver here. For both kinematics, the wing model was initially accelerated at $0.03\,\text{m}/\,\text{s}^2$ to reach the steady traverse velocity of $0.1\,\text{ms}^{-1}$. Then the wing model was towed forward at this steady velocity for at least 2 chord lengths, to achieve the steady flow around the wing model, before the start of the landing flight. The Re, based on U_∞ and $c = 0.1$ m, was 13 000. Also, the wings were oriented at an initial AoA, $\alpha_0 = 15^\circ$, during the steady part of the motion. However, during the heave-only or heave-pitch case, the effective angle of attack (α_{eff}) was changed as

$$\alpha_{\text{eff}} = \alpha_0 + \arctan\left(\frac{-\dot{h}}{U_\infty}\right) + \alpha(t), \tag{1}$$

where $\dot{h}$ is the heave velocity, and $\alpha(t)$ is the pitch angle. The resultant motion profiles of these two kinematics are shown in Fig. 3. The kinematic parameters governing the overall motion of the foil are summarized in Table I. At the end of both kinematics, the nondimensional ground height clearance, $\acute{h}$, was fixed to a value of 0.2.

TABLE I. Kinematic parameters.

Parameter	Heave-only	Heave-Pitch	Unit
Traverse velocity (U_∞)	0.1	0.1	m/s
Traverse acceleration ($\dot{U}_\infty$)	0.03	0.03	m/s^2
Heave velocity($\dot{h}$)	0.05	0.05	m/s
Heave acceleration($\ddot{h}$)	0.12	0.12	m/s^2
Pitch rate ($\dot{\alpha}$)	0	15	deg/s
Pitch acceleration($\ddot{\alpha}$)	0	36	deg/s^2

C. Measurements of instantaneous forces

The instantaneous forces on the wings were measured with a six-axis force and torque sensor (MINI 40, ATI Inc., USA) connected to a 16-bit DAQ device (NI-USB-6211, National Instrument, USA). Force-sensor data were acquired at a sampling rate of 5 kHz, and they were averaged over five runs. The oscillatory frequency on the force-sensor data due to the vibration caused by the plunging motor was around 4 Hz. To remove this vibration, the force data were filtered with a Butterworth low pass filter with a cutoff frequency of 3 Hz. This filtering process was found to remove the contamination of the structural vibration on the measured force data but at the same time retain most of the oscillatory peaks due to fluid forces. Thereafter, a moving average of 20 points was used to further smooth the data. The uncertainty in the force data is found to be around 7% at the peak and less than 4% for the smaller magnitude of the forces.

Both dynamic and static tare were performed to account for the effect of inertial forces and the weight of the wing assembly. For dynamic taring, the tare experiments were conducted in the air by carrying out the same kinematics as in the water. When the dynamic tare data was compared with the measured force data, the lift force in water was approximately 11 times higher than the lift force in the air. If the apparent mass of the water accelerated along the model is approximately 10 times higher than the mass of the model and the force balance, we can neglect the dynamic tare in air [10,24]. For static taring, we measured the data in still water at every 3° of the pitch angle up to the maximum pitch angle attained during the heave-pitch kinematics. In the present study, the wing model produced negligible static tare. For this reason, we neglected the contribution of static tare in the force data.

D. Flow-field measurements

Planar particle image velocimetry (PIV) was used to measure the velocity field at two separate planes located at the (1) 50% span and (2) 70% span of both the wings. The water tank was seeded with neutrally buoyant, silver-coated hollow glass spheres (Conductophill, Potter Inc., USA) of 10 μm diameter. The plane of interrogation was illuminated by a laser sheet generated using a continuous-wave green laser (FN Series, Dragon laser Ltd., China). The laser head generated a beam with a diameter of 2 mm, which was expanded into a 2 mm thick laser sheet by using two cylindrical lenses. Images were recorded with a CCD camera (PCO2000, PCO Tech, USA) at a frame rate of 200 Hz and a resolution of 1280×1024 pixels. The field of view was 0.4×0.32 m. The images were processed in PIVLab, a MATLAB-based software. We used an iterative multi-pass algorithm with a window size of 64×64 pixels in the first pass and 32×32 pixels in the second pass, with a 50% overlap between each successive window. PIV data were phase-averaged over five runs.

To calculate the circulation inside the leading-edge and trailing-edge vortices, we used two scalar functions Γ_1 and Γ_2, following Graftieaux *et al.* [25]. The dimensionless scalar function Γ_1 identifies the vortex core, whereas the dimensionless scalar function Γ_2 detects the vortex boundary. The scalar function Γ_1 and Γ_2 is defined as

$$\Gamma_1(p) = \frac{1}{N}\sum_{i=1}^{N}\frac{[(x_p - x_i)\times u_i]n}{\| x_p - x_i \| \cdot \| u_i \|}, \tag{2.1}$$

$$\Gamma_2(p) = \frac{1}{N}\sum_{i=1}^{N}\frac{[(x_p - x_i)\times (u_i - \overline{u}_p)]n}{\| x_p - x_i \| \cdot \| u_i - \overline{u}_p \|}, \tag{2.2}$$

where p is a fixed point in the two-dimensional domain. $\mathbf{x}_i$ is the position vector, $\mathbf{u}_i$ is the velocity vector, and N is the total number of points in the flow domain. $\mathbf{n}$ is the unit vector normal to the plane. In this study, a threshold value of $|\Gamma_1| > 0.9$ was applied, and the location of the vortex core was determined by the maximum local value of Γ_1. The maximum value of Γ_2 represents the vortex boundary. Here, a threshold of $|\Gamma_2| > \frac{2}{\pi}$ was used to represent the vortex boundary. After the

vortex contour is identified, the vorticity within this vortex boundary was summed up to compute the circulation inside that contour.

E. CFD simulations

A commercial software code, STAR-CCM+ [26], was used to numerically simulate the flow of water over the rectangular and the swept plate during both the kinematics. This software uses a SIMPLE-C segregated solver with second-order special accuracy. The numerical simulations were solved based on the Navier-Stokes equations for the conservation of mass and momentum. The fluid was assumed to be isothermal, laminar, and have a constant density. With these assumptions, the reduced conservation equations used in simulation are expressed as

$$\frac{\partial u_i}{\partial x_i} = 0, \tag{3.1}$$

$$\frac{\partial u_i}{\partial t} + \frac{\partial u_i u_j}{\partial x_i} = -\frac{1}{\rho}\frac{\partial p}{\partial x_i} + \nu \frac{\partial^2 u_i}{\partial x_i^2}. \tag{3.2}$$

The motion of the wings was simulated using the overset mesh schemes, which utilize the sliding meshes to solve for the solid body displacement. A no-slip boundary condition was used on the wing and floor boundary to capture any viscous vortex shedding interactions occurring with the floor boundary to replicate a true ground effect phenomenon. A symmetry plane boundary condition was applied on the side walls to avoid any fluid effects that could arise due to the wall boundary. In the experiment, the wing was just under the water surface. Thus, our numerical model does not exactly replicate the experimental procedure; however, we assumed that the water-boundary effects were minimal and thus can be simulated using a symmetry plane boundary condition.

To compute the numerical uncertainty due to the mesh size, we carried out a mesh-independence sensitivity study. We systematically varied the mesh base size and time step to maintain a constant Courant number of unity. The rectangular wing with the heave-pitch kinematics was considered for this mesh-independence study. Based on this study, for all the cases, we used a mesh base size of 0.002 m and an appropriate time-step of 0.005 s. The time-step which resulted in the best match with the experimental data was selected for further analysis.

F. Analytical modeling of unsteady lift

1. Added mass force

Added mass or noncirculatory force contributes to the change in unsteady forces during the acceleration or deceleration of the fluid. Following Polet *et al.* [2], the noncirculatory force coefficient for a decelerating, heaving, and pitching plate is determined from the following equation:

$$C_{F_{\text{nc}}} = \frac{\pi c}{2U_\infty^2}[\ddot{h}\cos(\alpha) + \dot{\alpha}\cos(\alpha)U + \sin(\alpha)\dot{U} + c\ddot{\alpha}(1/2 - x_p^*)]. \tag{4}$$

Equation (4) shows that four distinct factors influence the noncirculatory force coefficient. The first term on the right-hand side of Eq. (4) is related to the heaving acceleration, $\ddot{h}$, the second term represents the rate of change of the added mass, the third term is related to the added mass due to linear acceleration, and the last term represents the added mass due to rotational acceleration, $\ddot{\alpha}$. Here, $(1/2 - x_p^*)$ is the relative distance between the midchord and the hinge location, which is zero in the present case.

The resultant noncirculatory lift and drag coefficient is defined as

$$C_{L_{\text{nc}}} = C_{F_{\text{nc}}}\cos(\alpha), \tag{5.1}$$

$$C_{D_{\text{nc}}} = C_{F_{\text{nc}}}\sin(\alpha). \tag{5.2}$$

2. Circulatory force

During both the kinematics, the circulatory forces (F_c) were calculated by simply considering the time derivative of the hydrodynamic impulse (I) caused by the counterrotating LEV, TEV pair [27]:

$$\frac{d\boldsymbol{I}}{dt} = \frac{d(\rho\Gamma\boldsymbol{d})}{dt}, \tag{6}$$

$$\boldsymbol{F}_c = -\rho\Gamma\dot{\boldsymbol{d}} - \rho\dot{\Gamma}\boldsymbol{d}, \tag{7}$$

where Γ is the circulation of one of the vortices, $\dot{\Gamma}$ is the time rate of change of circulation, $\boldsymbol{d}$ is the distance between the center of counterrotating vortices, and $\dot{\boldsymbol{d}}$ is the relative velocity between the two vortices. Equation (7) indicates that the unsteady circulatory force is composed of convection of the LEV relative to the TEV and the growth rate of the circulation inside these vortices. We calculated the centroid and the circulation of the vortices at different instants from the PIV data by applying the Γ_1 and Γ_2 criteria. The circulatory lift coefficient is expressed as

$$C_{L_c} = -\frac{2}{U_\infty^2 c}[(u_{\mathrm{LEV}} - u_{\mathrm{TEV}})\Gamma + (x_{\mathrm{LEV}} - x_{\mathrm{TEV}})\dot{\Gamma}]. \tag{8}$$

Finally, the total lift coefficient from the analytical model is defined as

$$C_{L_{\mathrm{tot}}} = C_{L_{\mathrm{nc}}} + C_{L_c}. \tag{9}$$

The noncirculatory and circulatory forces defined in this analytical model are two-dimensional force coefficients. In the next section, we compare this two-dimensional force with the three-dimensional force produced on the finite perching wing. Although the two-dimensional model is not appropriate for the three-dimensional finite wing perching problem, this model provides an important insight into the distribution of the unsteady forces on the plate performing unsteady perching motion.

III. RESULTS AND DISCUSSION

In this section, we first compare the force histories—obtained from the force sensor as well as the numerical simulation—of both the "heave-only" and the "heave-pitch" cases (Sec. III A). Next, in Sec. III B, we present the vorticity field obtained from the experiments and simulations. Then in Sec. III C, we compare the results from the analytical model with the experimental data. Finally, in Sec. III D, we explain the 3D topology of the vortices developed on both plates during each kinematics.

A. Instantaneous forces

Figure 4 shows the evolution of the lift coefficient (C_L) with nondimensional time (t^*) on the rectangular and the swept wing during the heave-only and heave-pitch cases. The start of the towing motion is denoted by $t^* = 0$. At $t^* = 6$, the wing starts decelerating from a constant speed, U_∞. The heaving motion for the heave-only case and the combined heaving and pitching motion for the heave-pitch case also start at $t^* = 6$.

Figure 4 shows that during the steady motion, $t^* = 5.5$–6.0, the lift coefficient on the wing is reliant on the wing planform shapes. During this phase, the swept wing produces approximately 20% higher lift forces compared to the rectangular wing. It is to be noted that both the plates had the same planform area. The higher lift for a plate with a leading-edge curvature has also been noted by Hartloper and Rival [5] and was attributed to a more stable LEV. After $t^* = 6$, when both the kinematics are initiated, the lift coefficient experiences a steep rise and reaches the peak value at $t^* = 6.6$. This initial rise in the lift coefficient is mainly related to a noncirculatory and inertial-type force caused by the initial acceleration of the heaving motion in the heave-only case and to both the heaving and pitching acceleration in the heave-pitch case. These initial accelerations are related to

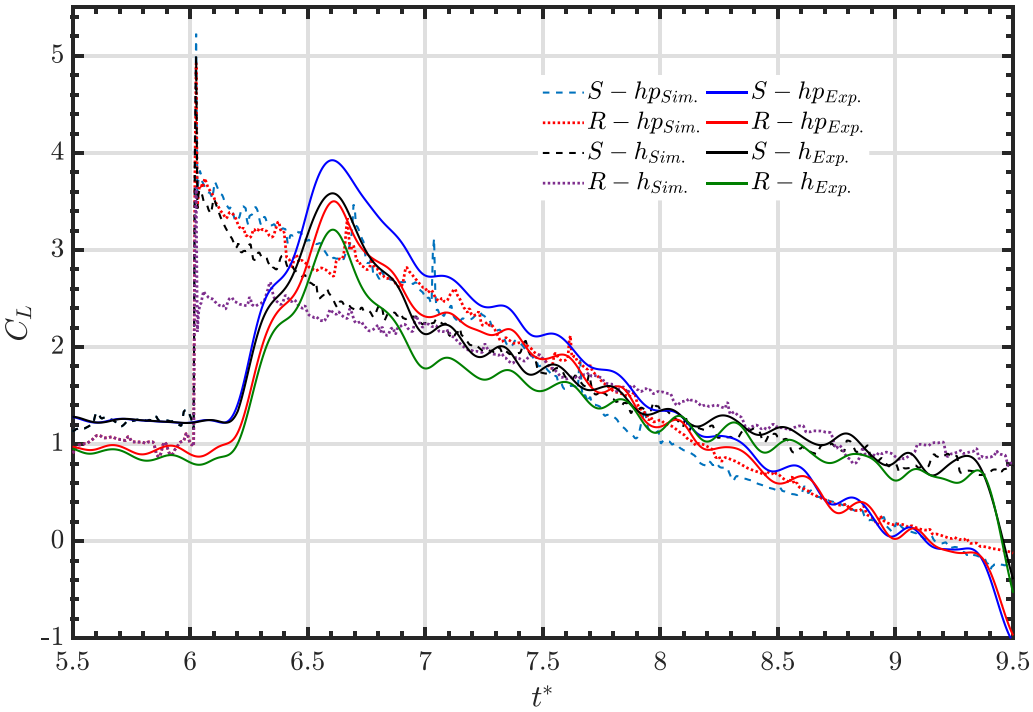

FIG. 4. Comparison of the lift coefficient on the rectangular, R, and the swept, S, wing planforms between the experiment, Exp., and simulation, Sim., data. The letters h and hp indicate heave-only and heave-pitch motion, respectively.

the start of the linear stage responsible for heaving and to the rotary stage responsible for pitching. When each of these stepper-driven stages starts from rest, they experience an initial acceleration to reach the desired speed. However, since the plates were at an AOA of 15°, an LEV and TEV were already present during the start of deceleration. Hence, these initial force peaks during the transient part of the motion can not be attributed to noncirculatory forces alone. Rather, we argue that the peaks around $t^* = 6$–6.5 are due to the combined effect of circulatory and noncirculatory forces, with a greater contribution from the latter.

A number of additional observations are made in Fig. 4. First, the C_L peaks from $t^* = 6.35$ to $t^* = 7.5$, for both the rectangular and swept plate, are relatively large in the heave-pitch case compared to the heave-only case. Higher magnitude in the peak force in the heave-pitch case corresponds to a larger noncirculatory force due to the addition of the pitch rate. Moreover, the wing in the heave-pitch case was operating at a higher effective AoA [Fig. 3(c)] than the wing under the heave-only case, which also contributed to higher lift forces. Next, during both kinematics, the C_L for the swept plate is always higher than the rectangular plate until $t^* = 7.5$. We argue that this higher C_L for the swept case during the unsteady phase is a direct consequence of the higher level of lift forces already present in the swept case during the steady phase, $t^* = 5.5$–6.0. Finally, the rate of the decay of lift force in the heave-pitch case was found to be higher than the heave-only case. This higher decay is also partly related to the high effective AoA in the heave-pitch case leading to a stalled flow at the latter half of the motion.

The results from numerical simulations are also presented in Fig. 4 as dotted (rectangular plate) and dashed line (swept plate). All the aforementioned observations are also evident in the numerical results, except for one significant difference. The increase in the C_L peak at the onset of the heave-only and heave-pitch kinematics occurs instantly compared to the gradual rise observed in

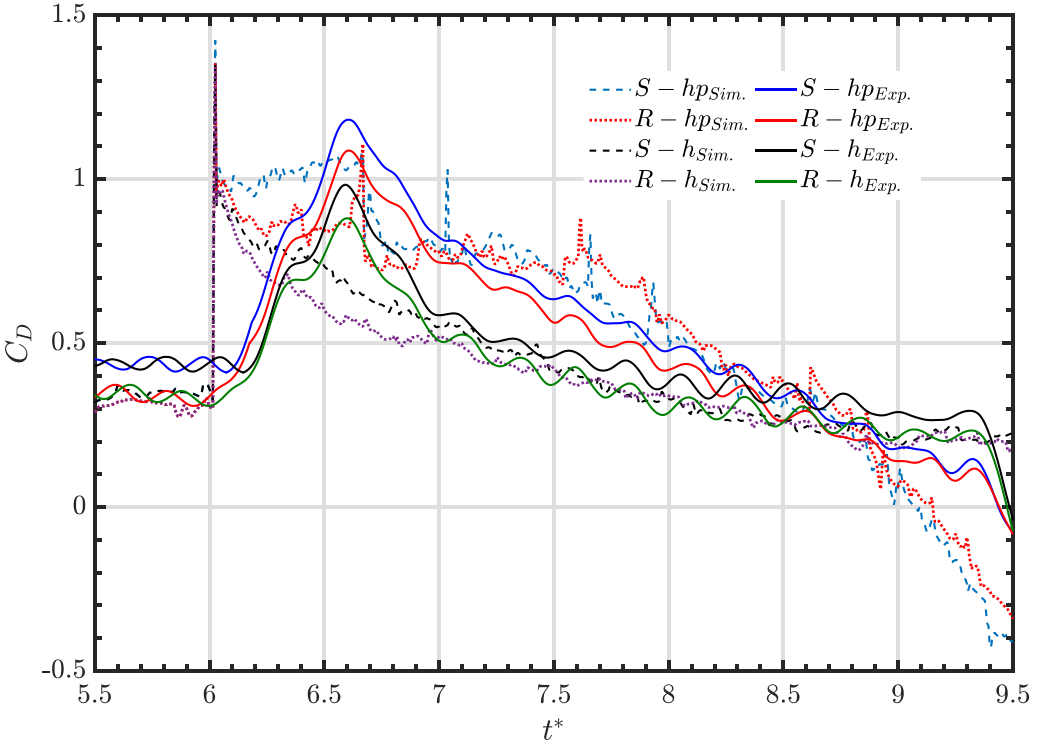

FIG. 5. Comparison of the drag coefficient on the rectangular, R, and the swept, S, wing planforms between the experiment, Exp., and simulation, Sim., data. The letters h and hp indicate heave-only and heave-pitch motion, respectively.

the experiment. This increase is due to the unsteady term in the Navier-Stokes equation which dominates due to the sudden change in velocity due to heaving or heaving and pitching kinematics. In the experiments, however, the increase in C_L is more gradual. This is mainly related to the finite time response of the force sensor to any step-change in the input.

The evolution of the drag coefficient (C_D) displays a similar trend observed in the lift coefficient (Fig. 5). The drag coefficient rises initially following the onset of the unsteady kinematics, attains a peak, and then decreases gradually. During the early phase of the maneuver, the drag coefficient is higher for the heave-pitch case than the heave-only case. This is mainly due to the higher effective AoA in the heave-pitch case, which caused a higher projected area facing the flow. For a safe landing, birds or flying vehicles must achieve a complete stop at the final phase of landing. Provini *et al.* [9] observed that birds generate most of the drag force from the wings than their legs during the last phase of the landing. It is interesting to note that the magnitude of the instantaneous drag coefficient is higher for heave-pitch case than the heave-only case. This higher drag force is favorable for the deceleration of the wing, which explains the reason why birds undergo rapid pitch-up motion during the landing flight. Note that the wing produces a negative drag force at the end of the motion, which is more pronounced for the heaving with pitching case. Negative drag or parasitic thrust at the end of the perching maneuver is supported by results presented in Polet *et al.* [2], where they concluded an increase in the added mass due to frontal area expansion could generate parasitic thrust at the end of the maneuver. However, the averaged drag coefficient from the pitch up motion is higher, which is essential for the safe landing motion.

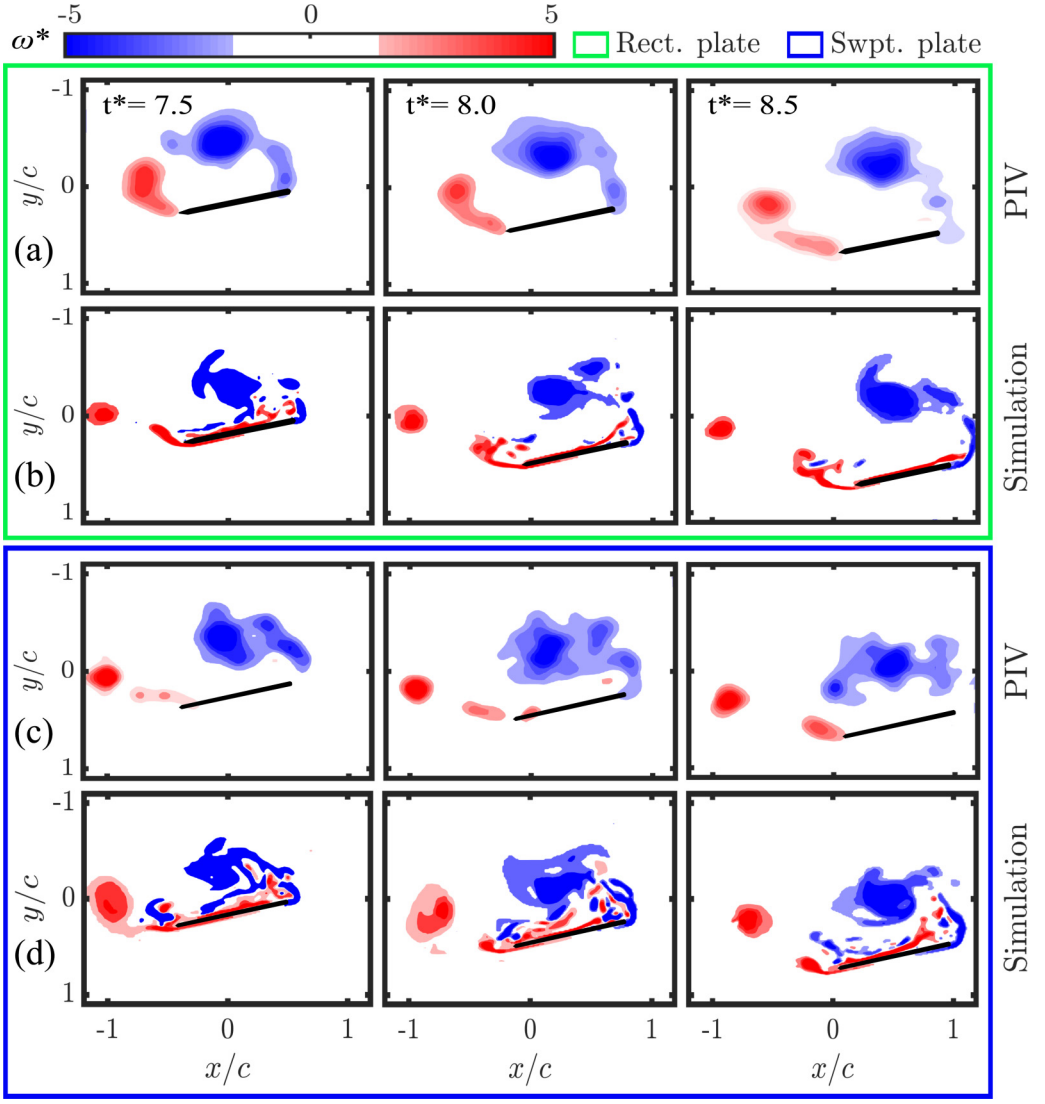

FIG. 6. Contours of the normalized vorticity field, ω^*, for the heaving motion at 50% of the wing span at various timesteps: (a) PIV results for the rectangular plate; (b) simulation data for the rectangular plate; (c) PIV results for swept plate; (d) simulation data for swept plate.

B. Flow features and development

We compare and contrast the normalized vorticity fields, ω^* ($= \frac{\omega * c}{U_\infty}$), over the rectangular and the swept plate, for both the kinematics, in Figs. 6–9. The vorticity fields were obtained at planes located at 50% and 70% span of the wing.

Figure 6 shows the vorticity field at the 50% span of the wing, obtained from both experiment and simulation during the heave-only case. The existence of a strong LEV (denoted by the blue contours representing negative vorticity) and a trailing-edge-vortex (TEV) (denoted by the red contours representing positive vorticity) is evident in these vorticity plots. During all the three time instants shown, the LEV formed on the rectangular plate has a more pronounced contour, whereas, for the swept plate, the vorticity contours are more diffused. Moreover, the center of the contour in the

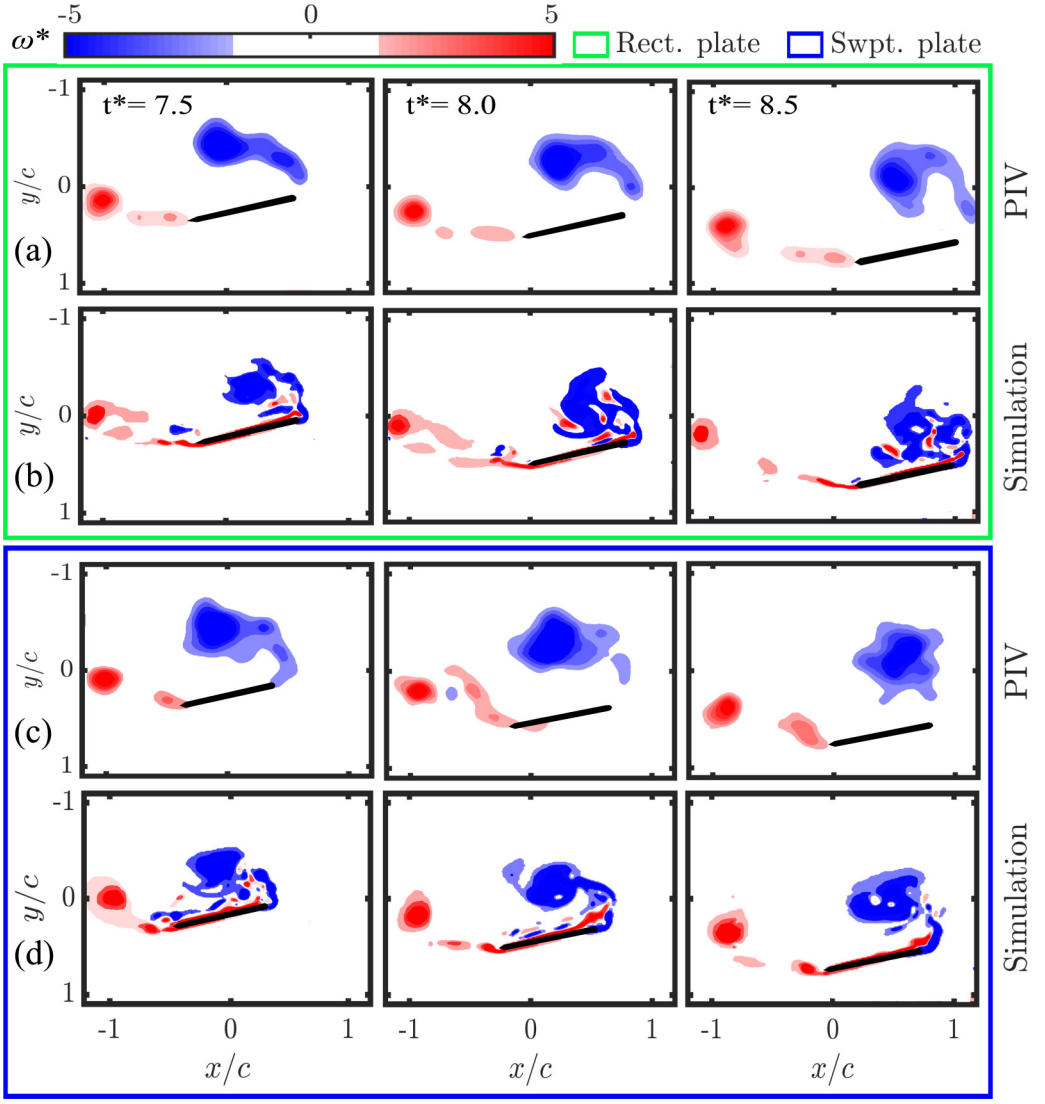

FIG. 7. Contours of the normalized vorticity field, ω^*, for the heaving motion at the 70% of the wing span at various time-steps: (a) PIV results for rectangular plate; (b) simulation data for the rectangular plate; (c) PIV results for the swept plate; (d) simulation data for the swept plate.

latter case appears closer to the heaving plate. We note that the simulation results contain boundary layer vorticity, which was not resolved in the experiment due to unwanted laser reflection. This boundary layer vorticity shows the development of the secondary vorticity (positive, red contours) behind the LE for both the kinematics. This secondary vortex weakens the connection between the LEV and the LE shear layer, which finally diminishes the mass flow from the feeding shear layer into the LEV. The vorticity plots obtained at the 70% span in the heave-only case show a reduced size for the contours in both the rectangular and swept plate cases (Fig. 7). However, one significant difference is that at 70% span, the contours in the swept case are more compact compared to the same obtained at the 50% span. These spanwise differences in the sizes of vorticity contours in both rectangular and swept plate cases prove that the cross-sections of the LEV are different based on

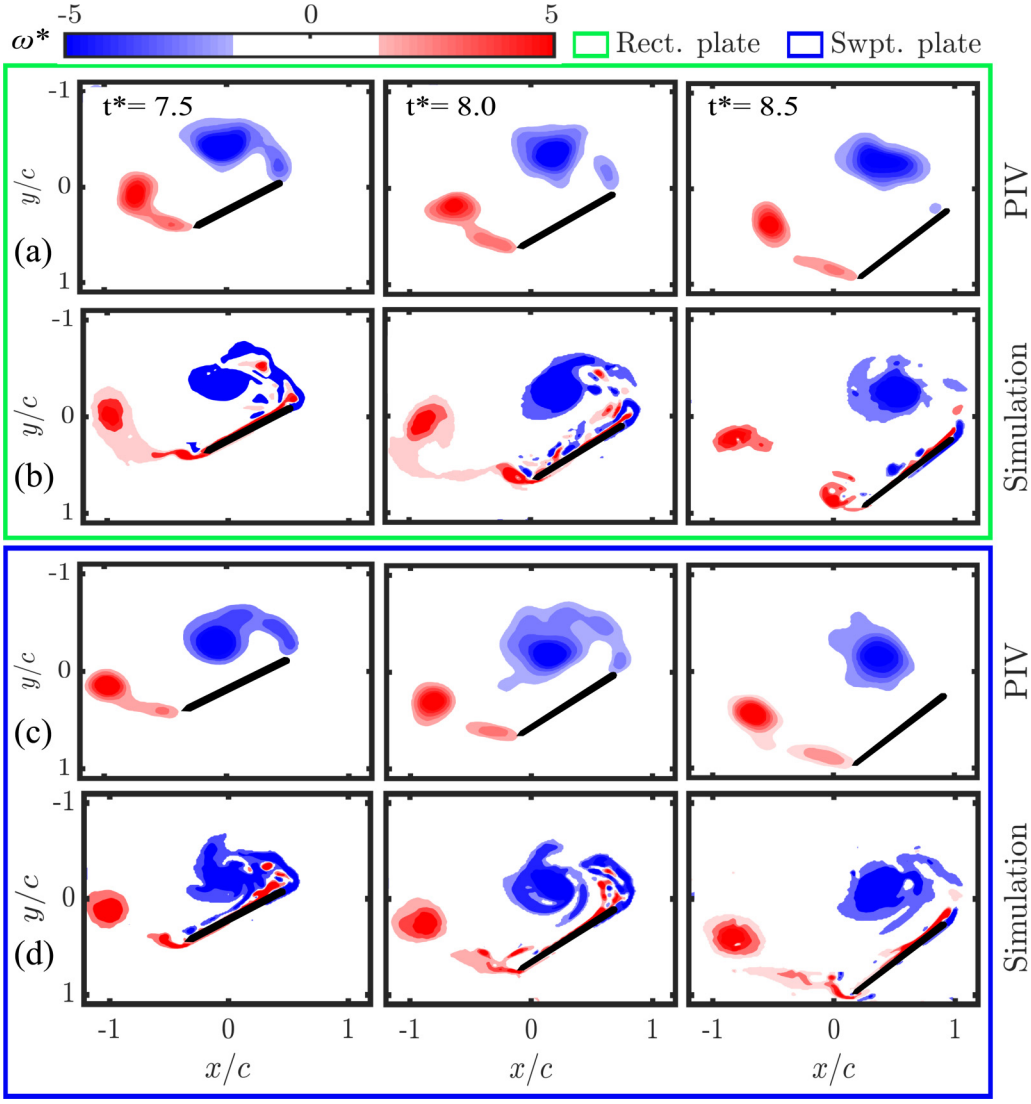

FIG. 8. Contours of the normalized vorticity field, ω^*, for the heave-pitch motion at the 50% of the wing span at various time-steps: (a) PIV results for the rectangular plate; (b) simulation data for the rectangular plate; (c) PIV results for the swept plate; (d) simulation data for the swept plate.

the span location. This difference also hints at a considerable degree of three-dimensionality in the flow.

The vorticity fields, at the 50% span, over both the plates in the heave-pitch case are shown in Fig. 8. The addition of pitching created smoother contours for the swept plate [Figs. 8(c) and 8(d)] compared to the heave-only case [Figs. 6(c) and 6(d)]. Another major difference is that the separated LEV ends up closer to the plate due to the higher effective angle of attack obtained in the heave-pitch case. When the plain of PIV was changed to the 70% span, similar well-defined vorticity contours were obtained (Fig. 9). For the heave-only case, although positive vorticity is observed behind the LE, there is still a weak connection between the LEV and LE shear layer even at $t^* = 8.5$ (Fig. 6). However, for the heaving with pitching case at $t^* = 8.5$, the LEV is fully detached from the feeding

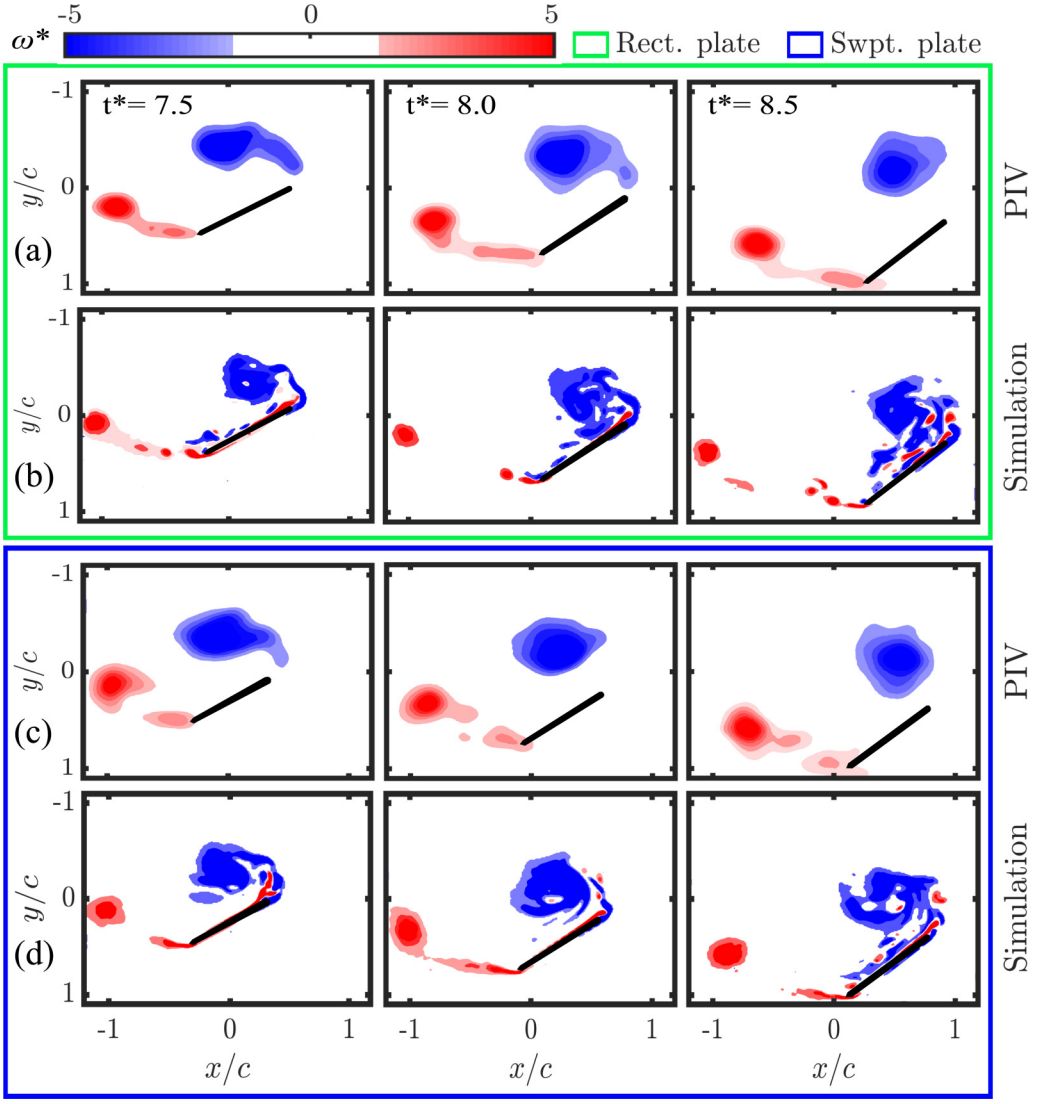

FIG. 9. Contours of the normalized vorticity field, ω^*, for the heave-pitch motion at the 70% of the wing span at various time-steps: (a) PIV results for the rectangular plate; (b) simulation data for the rectangular plate; (c) PIV results for the swept plate; (d) simulation data for the swept plate.

shear layer (Fig. 8). Li *et al.* [28] observed that secondary vortex forms earlier in the motion for larger α_{eff}, leading to the early detachment of the LEV from the feeding shear layer. This may explain the reason for the early detachment of the LEV and the rapid drop of the instantaneous forces (Figs. 4 and 5) for the wing in heaving and pitching motion.

A qualitative analysis of the vorticity plots between the heave-only and the heave-pitch cases shows that in the latter case, the contours are more defined, circular, and closer to the plate. Because of the pitch-up motion, the effective angle of attack of the wing is always higher than that of the heave-only motion. It has been observed that an increase in the effective angle of attack, α_{eff}, facilitates the feeding of the vorticity from the shear layer to the LEV during the early stage of the motion [28]. This continuous feeding of vorticity from the leading-edge leads to a pronounced LEV

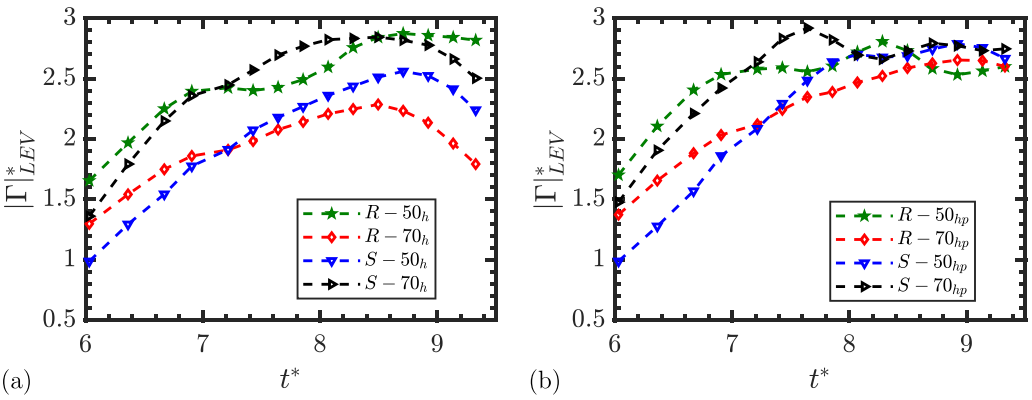

FIG. 10. Circulation history on the rectangular, R, and swept wing, S, at 50% and 70% of the wing span: (a) heave-only motion, h; (b) heave-pitch motion, hp.

(Figs. 8 and 9). A well-defined and larger LEV, located closer to the plate, is supposed to impart higher impulse on the plate in the heave-pitch case, which will increase the circulatory forces leading to higher lift forces compared to the heave-only case.

To compare the evolution of the LEV over the rectangular and the swept plate during both the kinematics, we plot the normalized circulation over time in Fig. 10. The circulation is computed using the Γ_1 and Γ_2 criteria on the velocity field obtained at planes located at 50% and 70% of the wing-span. For the swept-wing case, the circulation is higher at 70% than 50% of the wing-span during both the kinematics [Fig. 10(a)]. The sweep angle, in this case, creates a spanwise component of the incoming flow. This outward-directed flow convects the vorticity towards the tip. This spanwise convection of vorticity is responsible for the higher LEV circulation at 70% than 50% span. However, for the rectangular wing, the circulation is higher on the inboard section, i.e., at 50% span. Higher circulation value on the inboard section on the rectangular wing is also supported by Hartloper and Rival [5]. Figure 10 a also reveals that in the heave-only case, LEV circulation at the 70% span in the swept-plate case reaches the peak value at $t^* = 8.5$, whereas in the heave-pitch case, it reaches the peak value much earlier at $t^* = 7.5$. A similar observation is also made for the swept plate case at 50% span length. The higher value of LEV circulation for the wing in the heave-pitch case is consistent with the more compact vortices observed in the PIV results. An early peak at $t^* = 7.5$ and the subsequent plateau of the LEV circulation for the wing in the heave-pitch case is related to early pinch-off of the LEV from the plate (see Figs. 8 and 9). This finding also corroborates the higher rate of decay of lift forces in the heave-pitch case compared to the heave-only case (Fig. 4).

C. Decomposition of 2D aerodynamic load

In this section, we calculate the sectional lift at the midspan using analytical model defined in Sec. II F and compare them with the lift coefficients obtained from the experiment. Figure 11 shows that the noncirculatory forces were significantly higher during the starting and the end of the unsteady kinematics. However, these forces were negligible during the major part of the motion. Hence, it is evident that the majority of the lift was caused by circulatory forces. Figure 12(a) reveals that for the rectangular wing undergoing heaving motion, the analytical lift coefficient follows the experimental ones closely, especially, at the later part of the kinematics, at $t^* = 8$ and 8.5. The degree of deviation is more for the swept case. During the heave-pitch case [Fig. 12(b)], both the rectangular and the swept plate show considerable differences between the experimental C_L and that determined by 2D analytical modeling. This indicates that for the wing undergoing unsteady motion, the aerodynamic loads on the finite wing are not smoothly distributed along the wingspan.

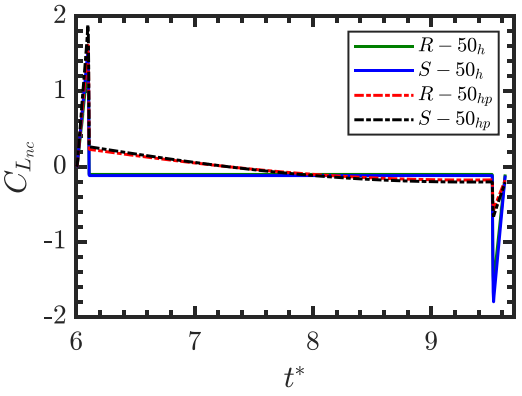

FIG. 11. Noncirculatory lift coefficient predicted from analytical model.

Here, the predicted lift force does not agree well with the experimental results. This difference can be explained qualitatively with the help of the three-dimensionality of the flow, which is the characteristic of the finite wing. To accurately capture the effect of such three-dimensionality (i.e., formation of tip vortex) on the resultant circulatory forces on the plate, we need to use 3D vortex force decomposition which requires volumetric data. 2D PIV data cannot capture the downwash effect of tip vortices, which affects the lift. For this reason, a low-order two-dimensional impulse method that uses 2D PIV data is expected to have discrepancies while predicting the circulatory lift. However, this method provides an important insight into the distribution of the aerodynamic load on the wing undergoing unsteady perching motion.

D. 3D flow structures

In this section, we use the CFD results to plot the 3D flow field around the rectangular and the swept plate undergoing the heave-only and the heave-pitch kinematics. Figures 13 and 14 show the isocontours of the pressure coefficient, C_P, and the isosurfaces of the z component of velocity, w. The isosurfaces of w are plotted using the Q criterion. We selected two time instants: Figure 13 represents the state of the flow field at $t^* = 7.5$, and Fig. 14 represents the same at $t^* = 8$. We note that $t^* = 7.5$ is located before the traces of the C_L in the heave-pitch case crossed that of the same in the heave-only case. However, $t^* = 8$ is located after this crossing point.

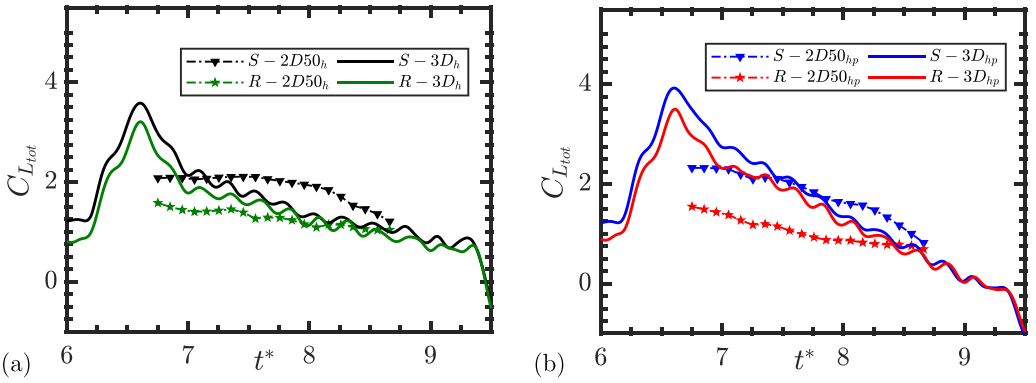

FIG. 12. A comparison between 3D lift coefficient from the experiment and 2D sectional lift predicted using added mass and 2D impulse method: (a) heave-only motion, h; (b) heave-pitch motion, hp. The symbol R and S indicates rectangular and swept planforms, respectively.

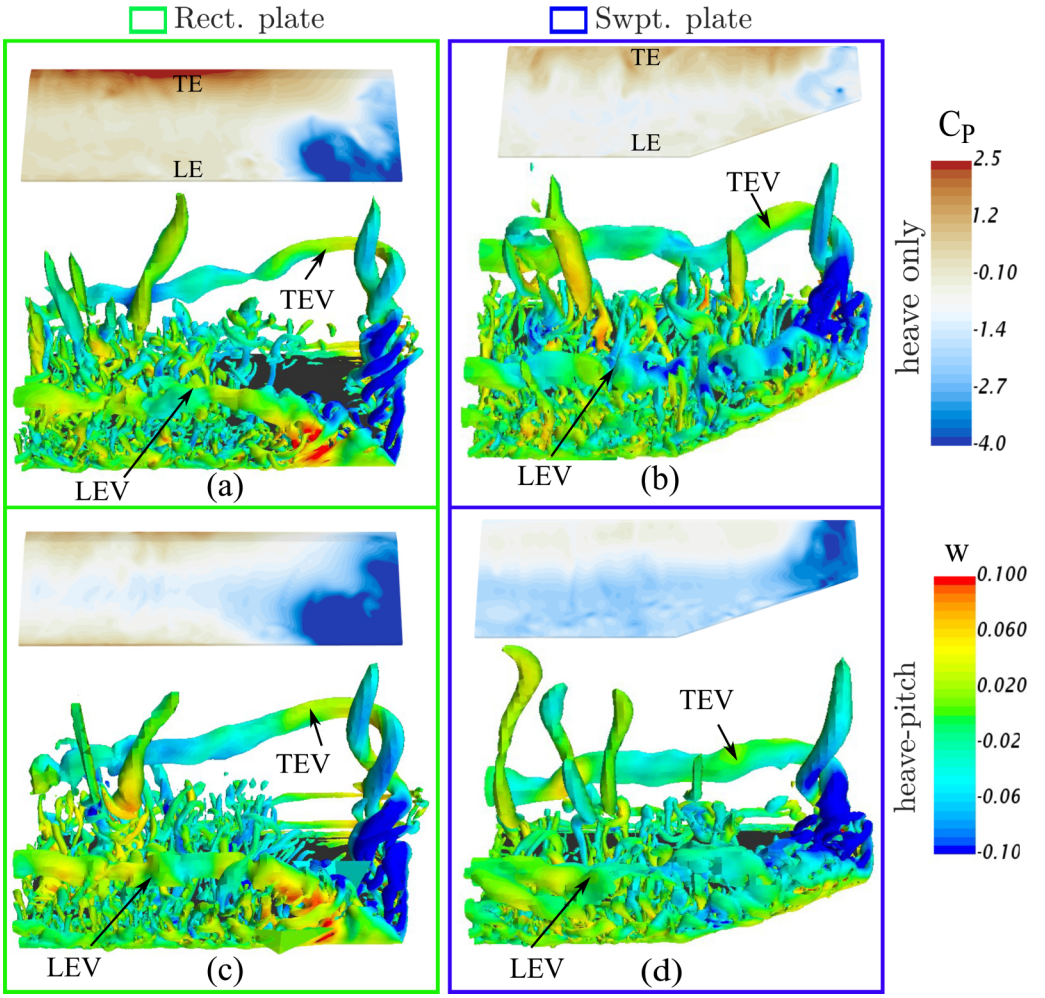

FIG. 13. Distribution of the pressure coefficient, C_P, on the wing suction surface (first and third row) and the isosurface representation of z velocity along the LEV and TEV using Q-criterion (second and fourth row) at $t^* = 7.5$: (a) rectangular wing in heave-only motion; (b) swept wing in heave-only motion; (c) rectangular wing in heave-pitch motion; and (d) swept wing in heave-pitch motion.

At $t^* = 7.5$, during the heave-only case, the LEV is pinned at the outboard section on the rectangular plate. The C_P is negative around the tip region where the LEV is pinned and also where the tip vortex is formed. One important observation is that the isocontours of w show an inward-directed spanwise flow from the tip to the root on the rectangular plate [Fig. 13(a)]. However, on the swept plate, the spanwise flow has a distinct negative component denoting flow towards the tip [Fig. 13(b)]. This outward directed spanwise flow is a direct result of the wing sweep, which creates a spanwise outward component of the incoming flow. This promotes the convection of vorticity from the inboard section towards the tip. This explains the reason behind the higher value of measured circulation at 70% than 50% span on the swept wing. In the heave-pitch case [Figs. 13(c) and 13(d)], the extent of negative C_P is higher on the wingspan for both the rectangular and the swept plate case. In the latter case, the negative C_P region is uniformly distributed along the leading edge, which proves that in the heave-pitch case, the LEV was located closer to the plate.

At $t^* = 8$, the LEV and the TEV are more lifted from both the plates. This is more evident in Fig. 14(b), where distinct outward spanwise flow is observed on the swept plate. The C_P contours

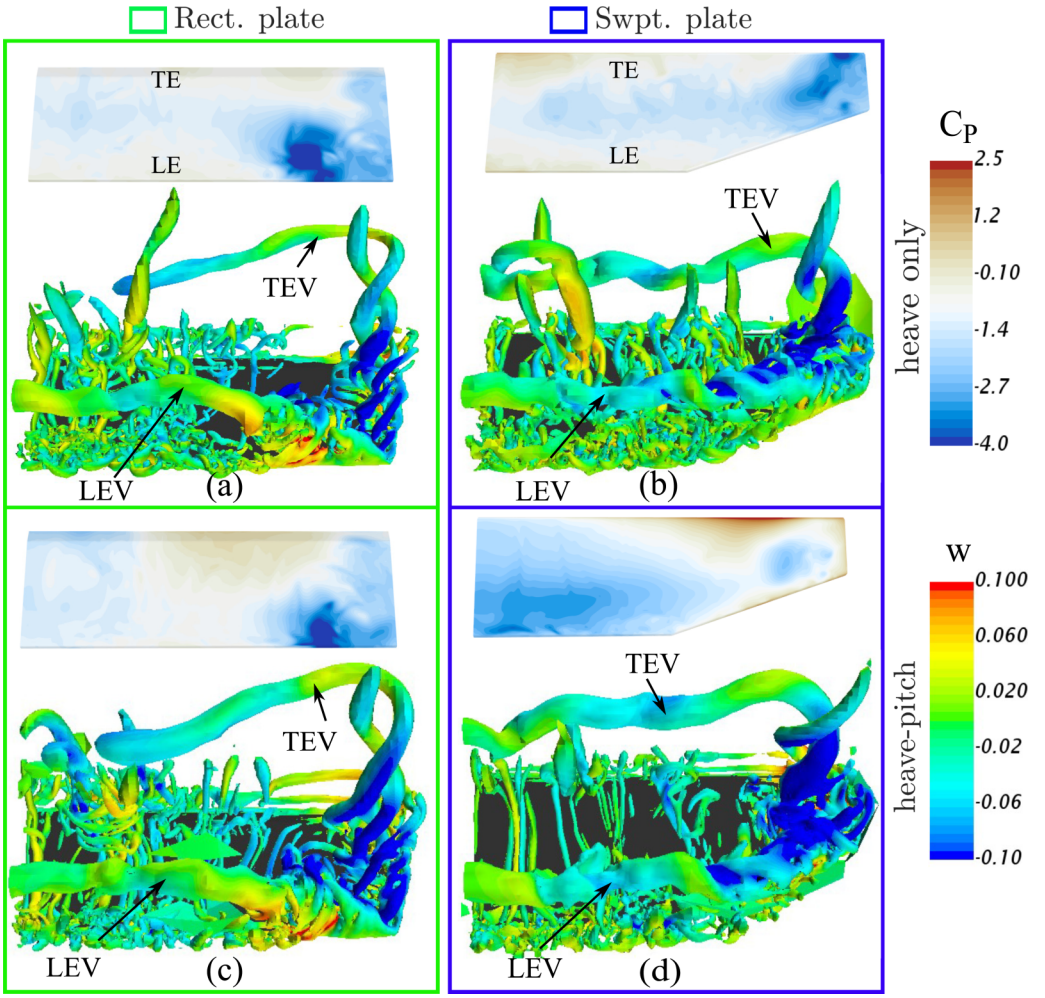

FIG. 14. Distribution of the pressure coefficient, C_P, on the wing suction surface (first and third row) and the isosurface representation of z velocity along the LEV and TEV using Q-criterion (second and fourth row) at $t^* = 8.0$: (a) rectangular wing in heave-only motion; (b) swept wing in heave-only motion; (c) rectangular wing in heave-pitch motion; and (d) swept wing in heave-pitch motion.

show that in the heave-pitch case, the swept plate has a higher region covered by negative C_P contours than the rectangular plate. Also, the TEV in both the rectangular and swept plate case appears to be more compact and has a bigger core diameter in the heave-pitch case compared to the heave-only case. A stronger TEV will result in a stronger downwash. This can explain why in the heave-pitch case, the lift rolls off rapidly at the later part of the kinematics (Fig. 4).

IV. CONCLUSION

Using experiments and simulations, we studied the unsteady forces and the flow field of a rectangular plate and a swept plate, undergoing heave-only and heave-pitch kinematics, to investigate the dynamics of a perching maneuver. In addition to heave or heave-pitch, the plates also decelerated to stop from a Re = 13 000. A simple analytical model, composed of added mass force and the

circulatory force, was also used to predict the instantaneous sectional two-dimensional lift force on both the plates and is compared with the experimental results.

For a safe landing, birds must produce enough lift force to support their weight and drag force to decelerate to a complete stop. In the present study, both the experiment and numerical simulation results showed that rapid pitch-up motion while heaving down during a decelerating flight enhances both the lift and drag forces on the wing. This higher value of lift and drag force is favorable for the safe landing, which explains the reason why birds undergo the rapid pitch-up motion during the landing flight. The heave-pitch motion also showed faster decay of the lift forces, which was attributed to faster pinching of the LEV from the plates. The swept plate experienced higher lift compared to the flat case in the heave-pitch case. The isocontours of C_P obtained from numerical simulation showed that in the swept plate case, the LEV was closer to the plate, causing a uniform distribution of negative C_P along the leading edge.

It was also found that LEV circulation was higher at 70% of the wingspan for the swept plate. Isosurface of the z velocity, w, revealed that in the presence of LE angle, an outward spanwise flow was induced in the swept wing. This promotes the convection of vorticity from the inboard section towards the tip resulting in a higher value of circulation on the outboard section for the swept wing. A simplified analytical model revealed that noncirculatory forces are important during the acceleration or deceleration part of heaving and pitching motion. Otherwise, the lift is contributed mostly by circulatory forces. To summarize, all these results indicate that wing-sweep does help in generating higher lift during perching.

ACKNOWLEDGMENTS

During the course of this research, D.R.A. was partially supported by a Office of Naval Research (ONR) (Grant No. N00014-18-P-1018), monitored by Dr W. Nickerson and later by National Science Foundation, CAREER award 2045767, monitored by Dr R.D. Joslin.

[1] A. C. Carruthers, A. L. R. Thomas, and G. K. Taylor, Automatic aeroelastic devices in the wings of a steppe eagle *Aquila nipalensis*, J. Expl Biol. **210**, 4136 (2007).

[2] D. T. Polet, D. E. Rival, and G. D. Weymouth, Unsteady dynamics of rapid perching manoeuvres, J. Fluid Mech. **767**, 323 (2015).

[3] G. D. Weymouth and M. S. Triantafyllou, Global vorticity shedding for a shrinking cylinder, J. Fluid Mech. **702**, 470 (2012).

[4] G. D. Weymouth and M. S. Triantafyllou, Ultra-fast escape of a deformable jet-propelled body, J. Fluid Mech. **721**, 367 (2013).

[5] C. Hartloper and D. E. Rival, Vortex development on pitching plates with lunate and truncate planforms, J. Fluid Mech. **732**, 332 (2013).

[6] K. Granlund, M. Ol, and L. Bernal, eds., *Experiments on Pitching Plates: Force and Flowfield Measurements at Low Reynolds Numbers* (AIAA SciTech, Orlando, FL, 2011).

[7] T. O. Yilmaz and D. Rockwell, Flow structure on finite-span wings due to pitch-up motion, J. Fluid Mech. **691**, 518 (2012).

[8] A. M. Berg and A. A. Biewener, Wing and body kinematics of takeoff and landing flight in the pigeon (*Columba livia*), J. Expl Biol. **213**, 1651 (2010).

[9] P. Provini, B. W. Tobalske, K. E. Crandell, and A. Abourachid, Transition from wing to leg forces during landing in birds, J. Expl Biol. **217**, 2659 (2014).

[10] K. O. Granlund, M. V. Ol, and L. P. Bernal, Unsteady pitching flat plates, J. Fluid Mech. **733**, R5 (2013).

[11] D. Rival, T. Prangemeier, and C. Tropea, The influence of airfoil kinematics on the formation of leading-edge vortices in bio-inspired flight, Exp. Fluids **46**, 823 (2009).

[12] Y. S. Baik, L. P. Bernal, K. Granlund, and M. V. Ol, Unsteady force generation and vortex dynamics of pitching and plunging aerofoils, J. Fluid Mech. **709**, 37 (2012).

[13] M. R. Visbal and J. S. Shang, Investigation of the flow structure around a rapidly pitching airfoil, AIAA J. **27**, 1044 (1989).
[14] T. Maxworthy, The formation and maintenance of a leading-edge vortex during the forward motion of an animal wing, J. Fluid Mech. **587**, 471 (2007).
[15] R. Blake, The energetics of hovering in the mandarin fish (*Synchropus picturatus*), J. Exp. Biol. **82**, 25 (1979).
[16] P. W. Webb, The effect of solid and porous channel walls on steady swimming of steelhead trout *Oncorhynchus mykiss*, J. Exp. Biol. **178**, 97 (1993).
[17] F. R. Hainsworth, Induced drag savings from ground effect and formation flight in brown pelicans, J. Exp. Biol. **135**, 431 (1988).
[18] J. M. Rayner, On the aerodynamics of animal flight in ground effect, Philos. Trans. R. Soc. B **334**, 119 (1991).
[19] J. M. Rayner and A. L. Thomas, On the vortex wake of an animal flying in a confined volume, Philos. Trans. R. Soc. B **334**, 107 (1991).
[20] R. V. Baudinette and K. Schmidt-Nielsen, Energy cost of gliding flight in herring gulls, Nature (London) **248**, 83 (1974).
[21] J. H. J. Buchholz and A. J. Smits, The wake structure and the thrust performance of a rigid low-aspect-ratio pitching panel, J. Fluid Mech. **603**, 331 (2008).
[22] E. Blevins and G. V. Lauder, Swimming near the substrate: A simple robotic model of stingrey locomotion, Bioinspir. Biomim. **8**, 016005 (2013).
[23] K. V. Rozhdestvensky, Wing-in-ground effect vehicles, Prog. Aerosp. Sci. **42**, 211 (2006).
[24] J. B. Barlow, W. H. B. Rae, W. H. Rae, and A. Pope, *Low-Speed Wind-Tunnel Testing*, 3rd ed. (Wiley, New York, NY, 1999).
[25] L. Graftieaux, M. Michard, and N. Grosjean, Combining piv, pod and vortex identification algorithms for the study of unsteady turbulent swirling flows, Meas. Sci. Technol. **12**, 1422 (2001).
[26] STAR CCM+ Users Manual (2018).
[27] H. Babinsky, P. R. R. J. Stevens, A. R. Jones, L. P. Bernal, and M. V. Ol, eds., *Low Order Modelling of Lift forces for Unsteady Pitching and Surging Wings* (AIAA SciTech, San Diego, CA, 2016).
[28] Z. Y. Li, L. H. Feng, J. Kissing, C. Tropea, and J. J. Wang, Experimental investigation on the leading-edge vortex formation and detachment mechanism of a pitching and plunging plate, J. Fluid Mech. **901**, A17 (2020).